

See discussions, stats, and author profiles for this publication at: <https://www.researchgate.net/publication/231646986>

# Gold Mining by Alkanethiol Radicals: Vacancies and Pits in the Self-Assembled Monolayers of 1-Propanethiol and 1-Butanethiol on Au(111)

ARTICLE in THE JOURNAL OF PHYSICAL CHEMISTRY C · MAY 2011

Impact Factor: 4.77 · DOI: 10.1021/jp111811g

CITATIONS

17

READS

49

6 AUTHORS, INCLUDING:



**Yun Wang**

Griffith University

89 PUBLICATIONS 1,149 CITATIONS

SEE PROFILE



**Qijin Chi**

Technical University of Denmark

98 PUBLICATIONS 2,299 CITATIONS

SEE PROFILE



**Noel Hush**

University of Sydney

309 PUBLICATIONS 11,574 CITATIONS

SEE PROFILE



**Jingdong Zhang**

Technical University of Denmark

100 PUBLICATIONS 2,297 CITATIONS

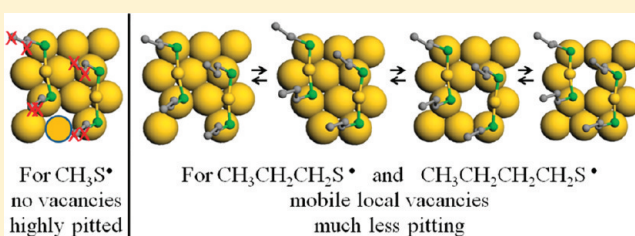
SEE PROFILE

# Gold Mining by Alkanethiol Radicals: Vacancies and Pits in the Self-Assembled Monolayers of 1-Propanethiol and 1-Butanethiol on Au(111)

Yun Wang,<sup>†,||</sup> Qijin Chi,<sup>‡</sup> Noel S. Hush,<sup>†,§</sup> Jeffrey R. Reimers,<sup>\*,†</sup> Jingdong Zhang,<sup>‡</sup> and Jens Ulstrup<sup>\*,‡</sup><sup>†</sup>School of Chemistry, The University of Sydney, Sydney 2006, Australia<sup>‡</sup>Department of Chemistry, Technical University of Denmark, DK-2800 Lyngby, Denmark<sup>§</sup>School of Molecular Biosciences, The University of Sydney, Australia<sup>||</sup>Centre for Clean Environment and Energy and Griffith School of Environment, Griffith University, Gold Coast, QLD 4222, Australia

## Supporting Information

**ABSTRACT:** Scanning-tunneling microscopy (STM) under electrochemical control (in situ STM) in aqueous solution, combined with a priori density functional theory (DFT) image simulations at room temperature, reveals the atomic nature of the interface between Au(111) and self-assembled monolayers (SAMs) of 1-propanethiol and 1-butanethiol. Use of single-crystal gold substrates allows for both high-resolution images of the surface cell internal structure and the evaluation of pit densities on large surface terraces, while room-temperature STM image simulations facilitate discrimination between possible atomic interface structures. For both adsorbates, the high-coverage  $c(4 \times 2)$  phase is identified as  $(3 \times 2\sqrt{3})-4$ , while the medium-coverage striped phase of 1-propanethiol SAMs is identified as  $(7 \times \sqrt{3})-4$ . All of these structures contain two adatom-bound adsorbates of the form  $RS-Au-SR$  ( $R = C_nH_{2n+1}S^\bullet$ ) per surface unit cell. The observed pit coverages of 2.8–4.0% are much less than those typically found for methanethiol SAMs (ca. 12–20%), indicating that one of the two gold adatoms per cell in 1-propanethiol and 1-butanethiol SAMs is extracted to form a local surface vacancy rather than a coalesced surface pit. The surface vacancy appears free to diffuse within each cell on the STM time scale, with only small STM image changes associated with vacancy localization. Significantly, the  $c(4 \times 2)$  phases of 1-propanethiol and 1-butanethiol SAMs give quite different STM images. 1-Butanethiol SAMs show characteristics similar to those of longer linear alkanethiols with four bright spots per cell, while the 1-propanethiol SAM displays five bright spots organized in a different pattern. These differences are rationalized by a more uniform vacancy distribution and rigid structure for 1-butanethiol SAMs, compared to the different diffusionally labile vacancy configurations and higher lateral S–C–C–C conformational flexibility found for 1-propanethiol. Also, the differences in interface structure from that of methanethiol SAMs are rationalized in terms of varying pit coalescence energies. These subtle differences underline the striking diversity in the electronic and molecular structural packing even within a single class of closely related molecular adsorbates.



## 1. INTRODUCTION

Thiol–gold self-assembled monolayers (SAMs) have attracted much attention owing to their potential applications in molecular electronics, as biosensors, and as “paddings” for efficient and robust protein film voltammetry.<sup>1–4</sup> While there have been many experimental and theoretical studies of thiol–gold SAMs, fundamental properties such as the atomic structure of the thiol–gold interface remain to be clarified. The sulfur–gold junction is one of the most important elements of a thiol–gold SAM, crucial, e.g., to the conductance of chemisorbed alkanethiols sandwiched by two gold electrodes.<sup>5</sup> During chemisorption, the thiol hydrogen is lost, leaving an electrically neutral alkanethiyl radical bound to the surface.<sup>6–9</sup> Originally it was assumed that such radicals are simply chemisorbed directly onto the unreconstructed Au(111) surface,<sup>2,6,10–16</sup> but as this

paradigm could not easily account for observed surface pitting, alternate structures were postulated.<sup>17</sup> Subsequently, theoretical predictions of the sulfur adsorption site based on the direct chemisorption model were found to differ significantly from that observed experimentally by spectroscopic means:<sup>14,18–21</sup> theory predicts the chemisorption site to lie between the surface fcc and bridge sites, while atop sites are observed. A variety of alternative binding models have been proposed,<sup>22</sup> the most successful of which has been a model with two chemisorbed alkanethiols attached to the surface as well as to a supersurface gold adatom.<sup>8,22–33</sup>

Received: December 13, 2010

Revised: April 15, 2011

Published: May 06, 2011

Direct observation using scanning-tunneling microscopy (STM) of adatom-bound adsorbates on Au(111) was first reported for methanethiol SAMs at low<sup>24</sup> and high<sup>23</sup> coverage under ultrahigh vacuum conditions. Subsequently, adatom-mediated motifs of various forms were directly observed in thiol-monolayer covered gold nanoparticles through X-ray diffraction experiments.<sup>34,35</sup> Recently, we reported direct observation of an adatom-bound alkanethiol SAM on Au(111) at high coverage from solution for the branched-chain alkanethiol 2-methyl-1-propanethiol, using STM imaging interpreted by high-level simulation techniques.<sup>8</sup> Independently, adatoms on the surface have been demonstrated by careful removal of the adsorbates<sup>26</sup> using hydrogen adsorption and desorption techniques.<sup>27</sup> However, we have also shown that another alkanethiol, *t*-butanethiol, forms monolayers to Au(111) just as originally envisaged without the need to raise supersurface adatoms.<sup>7</sup> The general principles controlling thiol monolayer structure are thus yet to be determined, though gold nanoparticles are known to strongly favor adatom-bound chemisorption through enhanced headgroup interaction with the distorted gold surface.<sup>9</sup>

Even for SAMs known to bind via adatoms such as those formed by methanethiol and ethanethiol, many details of the interface structure remain unclear. Such SAMs are revealing, as quantum mechanics/molecular mechanics (QM/MM) simulations indicate that the attractive component of van der Waals interaction between linear alkanethiol chains can be neglected when the number of carbon atoms in the chain is less than four,<sup>36</sup> enabling properties of the headgroup interaction to be readily revealed. At high coverage, some STM images for 1-butanethiol SAMs, both in aqueous buffer solution<sup>37</sup> and ex situ,<sup>38,39</sup> have been recorded, as well as high-resolution in situ images for 1-propanethiol SAMs,<sup>30</sup> but none of these have as of yet been interpreted in terms of the atomic structure of the interface. Further, the SAMs of short linear alkanethiols typically show a striped phase at medium coverage whose structure needs to be rationalized with those observed at high coverage.<sup>24,30,31,40–43</sup>

A variety of theoretical investigations of the atomic structure of adatom-mediated motifs for methanethiol and ethanethiol SAMs at full coverage have been performed.<sup>23,25,28,29,44–47</sup> Two adatom-mediated motifs have been predicted to bind per surface cell, with each adatom motif adopting either a *cis* or *trans* configuration of the C–S–Au–S–C atoms (the S–Au–S atoms are nearly colinear).<sup>29</sup> While *trans* structures are typically observed in STM images on surfaces,<sup>24,31</sup> the coexistence of several phases in the same scan with varying brightness contrasts is also known and could be associated with this type of structural flexibility.<sup>48</sup>

For reactions of thiols with the unreconstructed Au(111) surface, it is usually assumed that the supersurface gold adatoms come initially from the nearby surface area, perhaps forming local vacancies in the surface unit cell.<sup>7,8,17,23,46</sup> Such local vacancies may coalesce to form surface pits, and as pits are commonly observed on the surface, it is also often assumed that coalesced pits are the thermodynamically most stable state.<sup>17,25,28</sup> The proposed structural models for alkanethiol SAMs at high coverage postulate an adatom coverage of one adatom per six Au(111) surface atoms, 16.7%, and quantitative measurement of the actual pit coverage provides a direct measure of any local-vacancy coalescence.<sup>8</sup> However, quantitative analysis also requires consideration of the gold atoms liberated during the initial phase of chemisorption involving lifting of the Au(111) bare-surface

reconstruction. The bare-surface reconstruction involves 46 surface atoms (in two rows along the  $\langle 1\bar{1}0 \rangle$  direction of 23 atoms each) occupying 44 bulk-like positions<sup>30,49–52</sup> and so liberates 4.5% of a monolayer of Au atoms when it is lifted. This implies that the coverage of surface pits should be around 12.2% if complete coalescence occurs and no atoms are extracted from other possible sources such as step edges. Hence pit-coverage measurements on large terraces of single-crystal substrates can provide a quantitative measure of a key property of SAM interfaces.<sup>8</sup> High-resolution STM images of the structure of the surface cell can also be used to discriminate between proposed structural models if a means for predicting STM images from the models is available.

Interpretations of grazing-incidence X-ray diffraction data for methanethiol and 1-hexanethiol SAMs<sup>23,47</sup> at 170 K in ultrahigh vacuum have led to the conclusion that both directly bound and adatom-bound adsorbates are in rapid equilibrium on the STM time scale. While later works have discounted the details of their proposed SAM structure<sup>7,28</sup> and reinterpreted the experimental data,<sup>25</sup> observed pit coverages provide a ready quantitative measure of this type of effect; also, their general conclusion that an equilibrium involving different types of structures controls observed STM images at room temperature remains probable and requires further investigation.

Here, we extend high-resolution STM imaging of 1-butanethiol and 1-propanethiol SAMs at both medium and high coverage. STM in the electrochemical in situ mode is used, allowing the adjustable external potential to optimize image quality and resolution. This mode brings the resulting structural information to accord more closely than ex situ STM (in, e.g., air or UHV) with possible SAM applications such as promoters in protein film voltammetry, revealing the local microenvironment for the broad class of interfacial electrochemical electron transfer processes.<sup>4</sup> The use of single-crystal substrates possessing large Au(111) terraces exceeding 300 nm in size is also critical to accurate pit-coverage determination as adsorbates bind preferentially to terrace edges and other defects.<sup>30</sup> We emphasize the combination of this observed pit-coverage information with high-resolution STM imaging in determining the composition of the surface unit cell. These results are also interpreted using density functional theory (DFT) calculations of the SAM structure and associated STM image simulations at room temperature, revealing the atomic structures of the interfaces and their sensitivity to both thermal motion and chemical variation. A focus is the nature and origin of the different interface structures formed in the SAMs of methanethiol, 1-propanethiol, and 1-butanethiol.

## 2. METHODS

**2.1. Experimental Measurements.** 1-Propanethiol ( $\text{CH}_3\text{-CH}_2\text{CH}_2\text{SH}$ , 98%) was obtained from Sigma. The  $\text{NH}_4\text{Ac}$  buffer (5 mM, pH 4.6) was prepared from 5 M stock solution (Fluka, ultrapure). pH was adjusted by acetic acid (Aldrich, 99.7%). NaOH (0.1 or 0.5 M) solutions were prepared from 30% stock solution (Merck, ultrapure) and used for voltammetric measurements of reductive desorption. Absolute ethanol (ultrapure) was from Merck. Milli-Q purified water (18.2  $\text{M}\Omega\text{ cm}$ ) was used throughout. The Au(111) electrodes used in both electrochemical and STM measurements were homemade and pretreated before use as described.<sup>37</sup>

The SAMs were prepared by soaking freshly quenched Au(111) electrodes in, in most cases, aqueous solution containing 1-propanethiol or 1-butanethiol (1–5 mM) overnight, followed by thorough rinsing with Milli-Q water before measurements. Electrochemical measurements were performed using an Autolab system (Eco Chemie, Netherlands), with a three-electrode system containing a Pt counter electrode, a reversible hydrogen electrode (RHE) as the reference electrode, and a Au(111) working electrode. STM imaging was carried out using a PicoSPM system (Molecular Imaging Co.) equipped with a bipotentiostat for potential control of both the substrate and tip. The STM tips were prepared from W or Pt/Ir (80:20) wire by electrochemical etching and insulated with Apiezon wax to reduce or eliminate Faradaic currents.

**2.2. Computational Modeling.** All computations were performed using the Vienna ab initio simulation package (VASP).<sup>53</sup> The electron–ion interactions are described using the optimized relativistic Vanderbilt-type ultrasoft pseudopotentials.<sup>54,55</sup> A plane-wave basis set is employed to expand the wave functions with a kinetic energy cutoff of 400 eV. For the electron–electron exchange and correlation interactions, the functional of Perdew and Wang (PW91),<sup>56</sup> a form of the general gradient approximation (GGA), is used throughout. The Au(111) surface is modeled by a supercell consisting of a four-layer slab separated by a vacuum region of six-layer equivalent thickness. When the geometry is optimized, the top two atomic layers and the adsorbates are allowed to relax, while the lower two layers are fixed at the ideal bulk-like position (obtained using the lattice content  $a_0 = 4.18$  Å estimated at the same level of theory<sup>57</sup>). The methods proposed by Neugebauer and Makov et al. are used to correct for the surface dipole moment.<sup>58,59</sup> Monolayers at various coverages are modeled using  $(7 \times \sqrt{3})$  or  $(3 \times 2\sqrt{3})$  surface cells (see Figure 1) with the Brillouin-zone integrations for structures at  $T = 0$  as well as for all STM image simulations performed using Monkhorst–Pack grids of special points, with  $(2 \times 6 \times 1)$  and  $(4 \times 4 \times 1)$   $k$ -point meshes, respectively. These  $k$ -points meshes have been demonstrated to be sufficient for our purposes.<sup>7,60</sup> Molecular dynamics calculations<sup>61</sup> at room temperature ( $T = 300$  K) were performed using DFT-calculated forces evaluated at the  $\gamma$  point only and an energy cutoff of just 287 eV. Such crude approximations are commonly used in molecular dynamics simulations of interfaces,<sup>23,62</sup> and test calculations (see Supporting Information) indicate that key energetic and structural properties remain conserved. All calculations of chemisorbed monolayers were performed by ignoring spin polarization, as studies<sup>6</sup> on similar systems have indicated that the adsorbate–substrate interaction is strong and the effect of spin polarization weak.

While the clean Au(111) surface undergoes a  $(22 \times \sqrt{3})$  reconstruction,<sup>30,52</sup> thiol chemisorption lifts the reconstruction<sup>3,7</sup> during the early stages of chemisorption at quite low coverages. As all regular monolayer structures are observed only after the reconstruction is lifted, we do not consider this process but focus instead on binding to the unreconstructed surface. The computational methods used herein do accurately describe the reconstruction process, however.<sup>7</sup> Although all experimental results considered are obtained for aqueous solution, we model only monolayers under vacuum conditions. Since the alkanethiol tail groups are hydrophobic, no strong specific solvent interactions can arise, in contrast to the SAMs containing ionic tail groups (such as cysteamine) in which the solvation of the charged tail groups is critical.<sup>62</sup> Also, the thiyl rather than thiolate

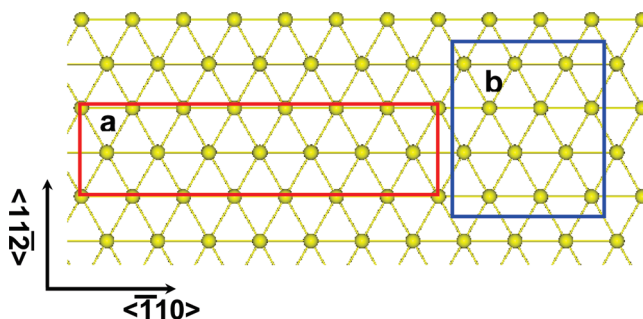


**Figure 1.** Au(111) surface cells used in the study. (a)  $(7 \times \sqrt{3})$  cell containing 14 regular surface gold atoms and (b)  $(3 \times 2\sqrt{3})$  cell containing 12 regular surface gold atoms.

nature of the headgroup means that the actual surface charge transfer is small, minimizing specific solvent interactions.<sup>60</sup> Large-amplitude thermal motions of the chains may still be influenced by the solvent structure, however.

STM images were simulated using the Tersoff–Hamann approximation based upon the local surface density of states (DOS).<sup>63</sup> We simulated images at constant density, mimicking observed STM images at constant current. To facilitate STM-image evaluation at high temperature, we note empirically that the main contributions to the partial DOS above the monolayer arise from the terminal groups of the adsorbates in thiol–gold SAMs.<sup>8,60</sup> Seven STM images calculated for disparate configurations extracted from the molecular dynamics simulations were simulated, and the calculated electron densities were fitted to the following interpolation functional form

$$\rho = \sum_i \alpha_i e^{-x_i/\beta_i} \quad (1)$$

where  $\rho$  is the partial DOS at each point in space well above the monolayer;  $x_i$  is the distance from such a point to atom  $i$ ; and  $\alpha_i$  and  $\beta_i$  depict the long-range falloff of the atomic electron density in the sampled voltage range. Details of this fit, including comparison of the original seven images and those re-evaluated using this interpolation, are described in the Supporting Information; the fitted parameters are:  $\alpha = 9.04 \pm 0.30$ ,  $\beta = 0.35 \pm 0.01$  for carbon and  $\alpha = 4.64 \pm 0.09$ ,  $\beta = 0.34 \pm 0.01$  for hydrogen. For each high-temperature simulated STM image reported, the STM images predicted using this approximation for 4500 configurations were averaged.

### 3. RESULTS AND DISCUSSION

**3.1. Low Coverage.** At low coverage, the Au(111) reconstruction can be lifted, but regular monolayers with resolved STM structure have not previously been observed for alkanethiol SAMs, despite, e.g., intensive searching for 1-propanethiol.<sup>30</sup> Indeed, no such SAMs are observed here for 1-butanethiol. However, SAMs at low coverage may be modeled theoretically. For 1-propanethiol SAMs, we consider the configuration with one adatom-mediated motif chemisorbed inside a  $(3 \times 2\sqrt{3})$  surface cell, corresponding to a coverage of  $\Theta = 1/6$  1-propanethiyl radicals per surface Au atom. This represents one-half of the coverage of a full monolayer and does not include significant intermolecular interactions. It is found that the predicted configuration of the adatom-bound adsorbate at this coverage is very similar to those deduced previously both experimentally and computationally at various coverages and



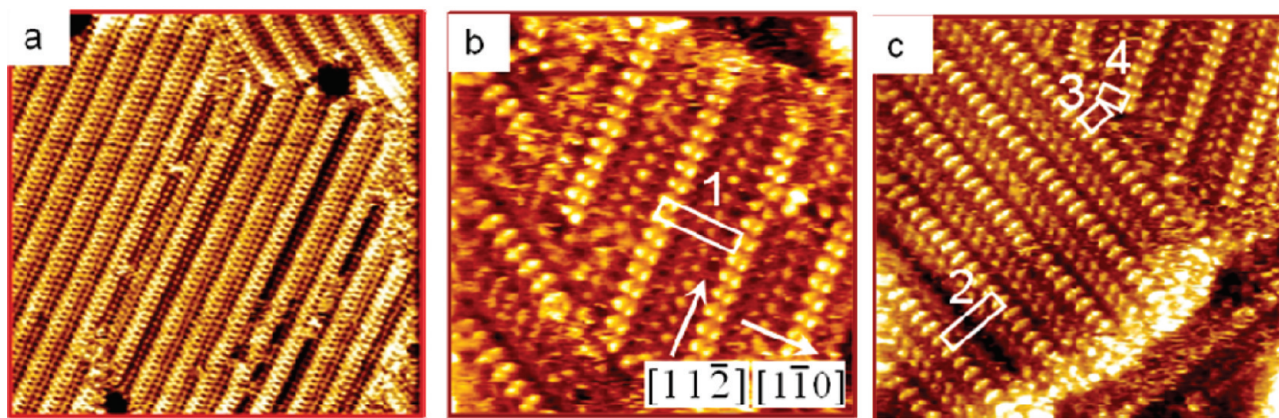


**Figure 2.** In situ STM images of the medium-coverage striped phase of the SAM of 1-propanethiol assembled on a single-crystal Au(111) surface, with the substrate lattice vectors indicated by the arrows. (a)  $50 \times 50$  nm, (b)  $8.5 \times 8.5$  nm, (c)  $13.5 \times 13.5$  nm. The structure of the most characteristic area, region 1, is shown enlarged in Figure 3, while grain-boundary and other anomalous structures are highlighted in regions 2–4. In situ STM images were obtained in 5–50 mM  $\text{NH}_4\text{Ac}$  (pH4.6), tunneling current 0.2–0.5 nA,  $V_{\text{bias}} = -0.13$ –0.2 V, and  $E_{\text{w}} = -0.3$  to 0.1 V versus SCE.

on nanoparticles.<sup>8,23–31,34</sup> In particular, we note that the energy of the *trans* or *cis* configurations is nearly identical.<sup>29</sup>

**3.2. Striped Phase at Medium Coverage.** The first stable phase of alkanethiol monolayers typically observed as the coverage increases is a striped phase.<sup>24,30–32,40–43</sup> No such phase is identified for 1-butanethiol SAMs, but Figure 2 shows such a phase for 1-propanethiol, with the stripes forming along the  $\langle 11\bar{2} \rangle$  direction.<sup>24,30,31,43</sup> In this figure, the absolute orientation of the substrate lattice is determined from the STM images of the single-crystal reconstructed Au(111) surface obtained before addition of 1-propanethiol. This SAM forms in the  $(7 \times \sqrt{3})$  lattice and contains 14 gold atoms per regular Au(111) surface layer in the unit cell.

Four regions in each unit cell are observed in the STM image of the 1-propanethiol SAM shown in Figure 3 that have strongly varying contrast: two bright spots close to each other and two dimer spots also close to each other; the spots are not collinear. These images are quite similar to those previously observed for 2-methyl-1-propanethiol SAMs on Au(111), SAMs that adopt the  $(8 \times \sqrt{3})$ -4 lattice.<sup>8</sup> As this phase forms at coverages less than that of the fully stable monolayer, it is not possible to determine the coverage independently by electrochemical means. For 1-propanethiol, it is possible that this phase is assembled with either one or two adatom motifs per  $(7 \times \sqrt{3})$  surface cell, indicating coverages of  $\Theta = 1/7$  and  $2/7$ , respectively. As large terraces are formed on the single-crystal substrates such as the one depicted in Figure 2a, the mining of gold atoms from step edges is minimized, and so it is possible to estimate the number of mined atoms purely from the pit coverage. The observed coverage of pits, averaging over Figure 2a and related images, is  $\sim 2.8\%$ . As 4.5% of a layer of gold atoms is released when the Au(111) surface reconstruction is lifted during monolayer formation, the coverage of adatoms above the surface is thus estimated to be  $0.028 \pm 0.045 = 0.073$ – $1/14$ . Hence, from the experimental data, it is clear that the striped phase must form in either (i) the  $(7 \times \sqrt{3})$ -2 lattice with one adatom-bound motif per cell, (ii) the  $(7 \times \sqrt{3})$ -4 lattice with two adsorbate radicals bound to an adatom and two bound directly to the surface, or (iii) the  $(7 \times \sqrt{3})$ -4 lattice with two adatom-bound motifs and one surface Au atom vacancy per cell.

To distinguish between these possibilities, conformations corresponding to the three structural models and their STM images at  $T = 0$  have been simulated, and the results are shown

in Figure 3b ( $(7 \times \sqrt{3})$ -4 lattice with 1 vacancy) and Figures 3c–e ( $(7 \times \sqrt{3})$ -2 lattice), where they are compared to region “1” of the observed STM image from Figure 2b. The optimized coordinates for these structures are also provided in the Supporting Information. Note that the  $(7 \times \sqrt{3})$ -4 lattice no-vacancy model is found to be clearly inconsistent with the observed images, and no results are shown explicitly. The predicted STM image for the  $(7 \times \sqrt{3})$ -2 structure has many features similar to the observed image, but significant subtle features are not reproduced such as the magnitude of the separation between the bright features and the number of weak features. Of note is the observation in Figure 2c of the region marked “2” in which a defect in the lattice occurs, the surface lattice taking on a local lower-density  $(8 \times \sqrt{3})$  region. A black stripe appears in this region, apparently indicating an uncovered region of the surface. The location of this black stripe is inconsistent with the basic properties of the  $(7 \times \sqrt{3})$ -2 model. Further, in the phase-boundary regions labeled “3” and “4” in Figure 2c, the structure is distinctly different from that shown in Figure 3a and suggests the presence of only enough matter to fill one-half of a surface cell. Hence, the only remaining viable option for the structure of the striped phase is a  $(7 \times \sqrt{3})$ -4 lattice at  $\Theta = 2/7$ .

Within the  $(7 \times \sqrt{3})$ -4 surface supercell, three unique possible locations exist for the surface gold-atom vacancy, as indicated in Figures 3c–3e; the calculated energies for these structures are essentially identical: the total difference is just 0.01 eV, much less than the likely accuracy of the calculation, and indicates no clear preference for any of the forms. Also, each structure has a simulated STM image that reproduces most features of the observed image. However, each structure predicts weak spots in roughly the same locations of the STM image, whereas spots in not only these locations but also other locations are actually observed.

The effects of thermal motion on the calculated STM images, obtained from 1.2 ps DFT molecular dynamics simulations at  $T = 300$  K, are also shown in Figure 3, while the calculated probability distribution functions for the Au–Au–S–C, Au–S–C–C, and S–C–C–C torsional angles at  $T = 0$  K and  $T = 300$  K are shown in Figure 4. Thermal motion over such a short time is predicted to have a profound effect on the torsional structure, making a wide range of alternate conformations available; indeed, the root-mean-square deviation of the horizontal motion of the carbon

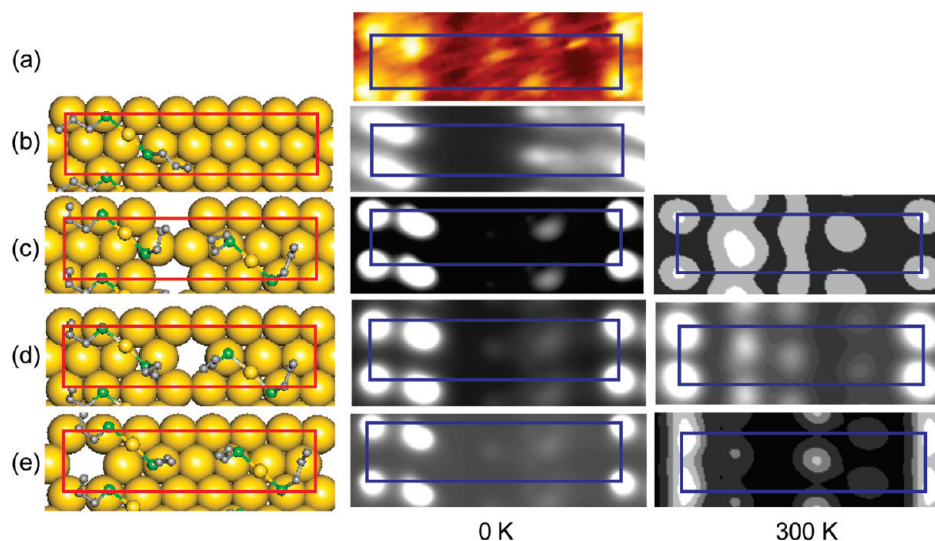


**Figure 3.** Striped phase of the SAM of 1-propanethiol on single-crystal Au(111): (a) experimental STM image at room temperature from Figure 2b, highlighting the  $(7 \times \sqrt{3})$  superlattice; (b) simulated STM image based on the optimized  $(7 \times \sqrt{3})$ -2 structure containing one adatom-mediated motif bound to the regular Au(111) surface; (c), (d), and (e) are simulated STM images for optimized  $(7 \times \sqrt{3})$ -4 structures, as well as those thermalized to  $T = 300$  K, containing two adatom-mediated motifs and one local vacancy per cell. Key: yellow, Au (large for surface layer, small for adatom); green, S; gray, C.

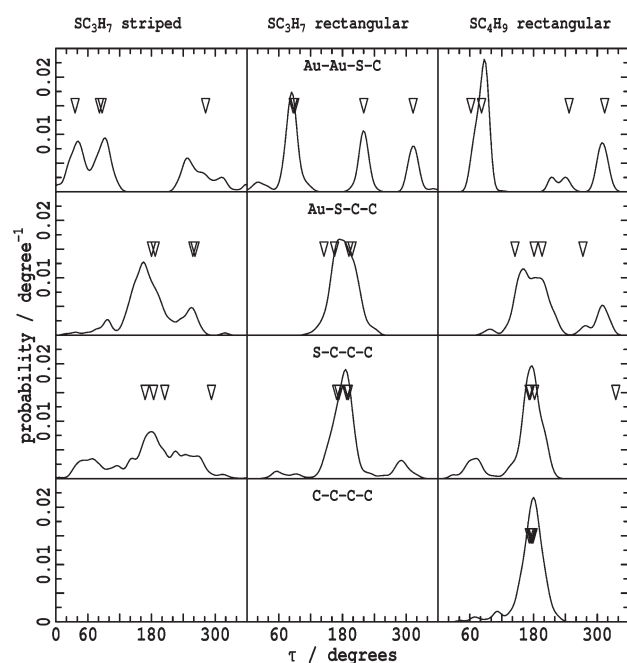


**Figure 4.** Calculated torsional angle probability distribution functions evaluated at  $T = 300$  K from 1.2 ps molecular dynamics simulations of SAMs on Au(111) performed using the PW91 density functional. Triangles indicate the values of the torsional angles in the corresponding optimized  $T = 0$  structures.

atoms is predicted to range up to 2 Å. Hence, the SAM presents more like a regular array of two-dimensional liquid droplets than as a rigid two-dimensional solid. Simulated STM images for seven snapshots of the structure shown in the Supporting Information give significant differences from the starting  $T = 0$  structure as well as between themselves. As a result, the simulated STM images at  $T = 300$  K develop additional features that correspond to the unanticipated features of the observed image. Such large-scale motions will interact with the solvent structure, and hence these simulations, performed in

the gas phase, could not be expected to quantitatively reproduce experimental data measured in electrolyte-containing aqueous solution. A clear scenario in which  $(7 \times \sqrt{3})$ -4 structures containing two adatom-bound motifs and one mobile surface vacancy account for all experimental observations is envisaged, however.

For methanethiol SAMs on Au(111), the striped phase is observed to be of slightly lower density (despite the smaller adsorbate size) with a  $(4 \times \sqrt{3})$ -1 structure without local vacancies.<sup>32</sup> The pit coverage is correspondingly much higher, estimated to be of the order of 16%.<sup>32</sup> However, a coverage of only 8% is expected for a  $(4 \times \sqrt{3})$ -1 structure of RS–Au–SR adsorbates, and the observed coverage may instead be taken as an indication of an alternate adatom-bound structure based on  $\text{CH}_3\text{SAu}$  adsorbates that appears inconsistent with other experiments.<sup>32</sup> For methanethiol SAMs,<sup>32</sup> the pits are typically very small, missing only of the order of 40 gold atoms, half of which could be considered to be at the edge of the pit. Interpretation of the appearance and extent of these pits in terms of the density of mined atoms is thus difficult, and it is possible that the pits appear twice the size that they actually are. Such problems are minimized for the pits of other alkanethiol SAMs as they are typically much larger in area (e.g., in Figure 2a over four times larger), and the adsorbate molecules are also much larger, facilitating accurate pit-coverage measurements.

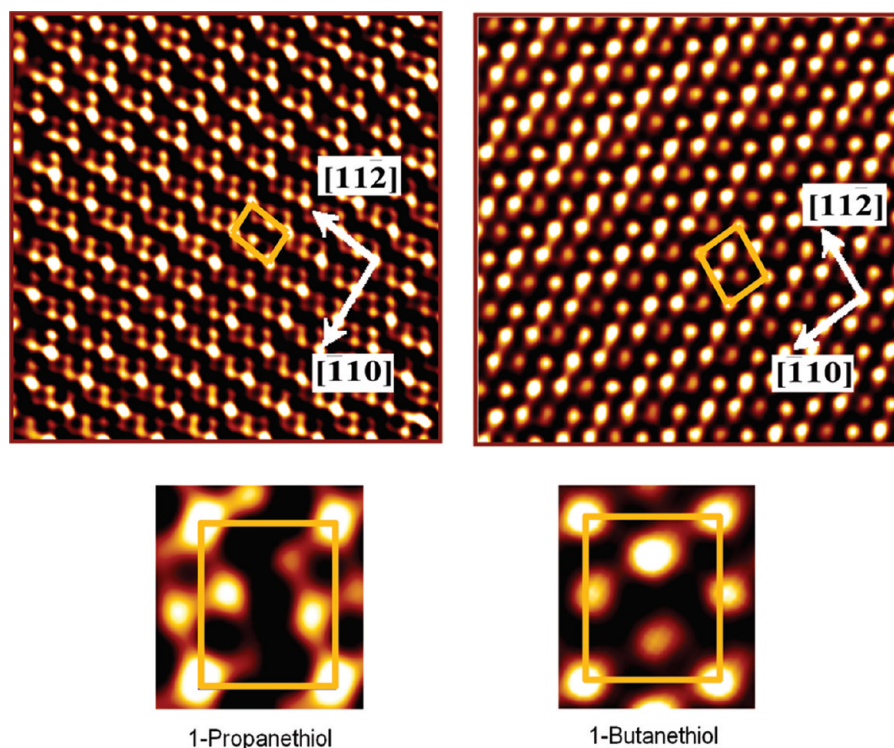
All simulated structures for the striped phase have *trans* C–S–Au–S–C conformations as only these lead to efficient packing of the adsorbates. This is in accord with experimental observations in which *cis* conformations are observed only at the end of stripes in boundary regions of striped-phase monolayers.<sup>31</sup> The deduced properties of the striped phase of 1-propanethiol and methylthiol SAMs are summarized in Table 1.

**3.3.  $c(4 \times 2)$  Rectangular Phase at High Coverage.** The observed STM images of 1-propanethiol and 1-butanethiol SAMs on Au(111) at high coverage are shown in Figure 5. Both SAMs form a rectangular phase with the  $(3 \times 2\sqrt{3})$ -4 lattice (or  $c(4 \times 2)$  lattice) at  $\Theta = 1/3$ , similar to the SAMs formed by methanethiol and ethanethiol. This coverage can be



**Table 1.** Summary of the Properties of Methanethiol,<sup>32,65</sup> 1-Propanethiol, and 1-Butanethiol SAMs at Different Coverage<sup>a</sup>

property	low coverage	striped phase		$c(4 \times 2)$ phase	
		methanethiol	1-propanethiol	methanethiol	1-propanethiol 1-butanethiol
pits coverage (%)	[0]	~16	2.8	12–20	4.0
thiol coverage (%)	[16.7]	25	28.6	33.3	33.3
lattice	$[(3 \times 2\sqrt{3})-2]$	$(4 \times \sqrt{3})-2$	$(7 \times \sqrt{3})-4$	$(3 \times \sqrt{3})-2$	$(3 \times 2\sqrt{3})-4$
adatom/cell	[1]	2	2	2	2
vacancy/cell	0	0	1	0	1
C–S–Au–S–C conformation	all	trans	trans	cis	cis
vacancy structure	—	—	mobile	—	mobile

<sup>a</sup> [ ] assumed in calculations.**Figure 5.** Observed high-resolution in situ STM images of the surface cells of the  $(3 \times 2\sqrt{3})-4$  substrate lattice of the 1-propanethiol SAM (left,  $9.4 \times 9.4$  nm) and 1-butanethiol SAM (right,  $8.0 \times 8.0$  nm) assembled on a Au(111) surface at a coverage of  $\Theta = 1/3$ . In situ STM images were obtained in 5–50 mM  $\text{NH}_4\text{Ac}$  (pH4.6), tunneling current 0.2–0.8 nA,  $V_{\text{bias}} = -0.13$  to 0.2 V, and  $E_w = -0.3$  to 0.1 V versus SCE.

determined independently of STM measurements at  $7.6 \pm 0.5 \times 10^{10} \text{ mol cm}^{-2}$  (or  $\Theta = 0.33 \pm 0.02$ ) for 1-propanethiol<sup>30</sup> and at  $7.8 \pm 0.3 \times 10^{10} \text{ mol cm}^{-2}$  (or  $\Theta = 0.34 \pm 0.01$ ) for 1-butanethiol,<sup>37</sup> calculated from the measured charge under the cathodic peak of the electrochemical reductive desorption peak<sup>64</sup> in 0.5 M NaOH. Previous theoretical studies on methanethiol and ethanethiol SAMs have proposed that this structure is composed of two adatom-mediated motifs per surface cell assembled on the regular Au(111) surface without surface vacancies, the C–S–Au–C–S linkages adopting *cis* configurations.<sup>28,29</sup> We consider not only this structure for 1-propanethiol and 1-butanethiol SAMs but also other structures containing either one or two local surface vacancies per substrate supercell.

The calculations reveal only one low-energy arrangement of the adsorbate molecules in a  $(3 \times 2\sqrt{3})-4$  lattice that is consistent with the experimental data for 1-propanethiol SAMs, but we consider 13 possible structures with one vacancy and 6 possible

structures with two vacancies. Results for the eight lowest-energy structures found are described in the Supporting Information, while Table 2 summarizes the implied pit coverage and calculated relative energy of the lowest-energy structure found of each type. Evaluating the relative energies of structures with different numbers of surface vacancies requires the determination of the energy for creation of a vacancy. Previous studies of this phenomenon have used the energy of a bulk gold atom for this purpose, defining the adsorption energy as<sup>23,28,46</sup>

$$\Delta E_B = (E_{\text{tot}} - E_{\text{surf}} - 4E_{\text{ad}} - nE_{\text{bulk}})/4 \quad (2)$$

where  $E_{\text{tot}}$  and  $E_{\text{surf}}$  are the optimized total energies of the systems with and without adsorbate, respectively;  $E_{\text{ad}}$  represents the energy of an isolated alkanethiyl radical;  $E_{\text{bulk}}$  is the average energy of gold atoms in the bulk; and  $n$  is the difference between the number of gold atoms in the surface cell and that in the corresponding regular

**Table 2.** For 1-Propanethiol and Methanethiol SAMs in the  $(3 \times 2\sqrt{3})$ -4 Lattice at High Coverage, Assuming 0–2 Local Surface Vacancies Per Cell, Are Shown the Calculated Energy of Binding Per Adsorbate Radical for the Lowest-Energy Structure of Each Type Found, Assuming That  $n$  Excess Gold Atoms Per Cell Are Taken from Either Bulk Gold,  $\Delta E_B$ , or Surface Pits,  $\Delta E_P$ <sup>a</sup>

no. of local vacancies	$n$	pits coverage (%)	1-propanethiol			methanethiol	
			no. of structures considered	$\Delta E_B$ (eV)	$\Delta E_P$ (eV)	$\Delta E_B$ (eV)	$\Delta E_P$ (eV)
0	2	12.1	1	−1.96	−1.87	−1.91	−1.80
1	1	3.8	13	−1.90	−1.86	−1.79	−1.73
2	0	4.5	6	−1.82	−1.82	−1.70	−1.70

<sup>a</sup> The observed pit coverage is ca. 4.0% for 1-propanethiol and 12–20% (see text) for methanethiol.

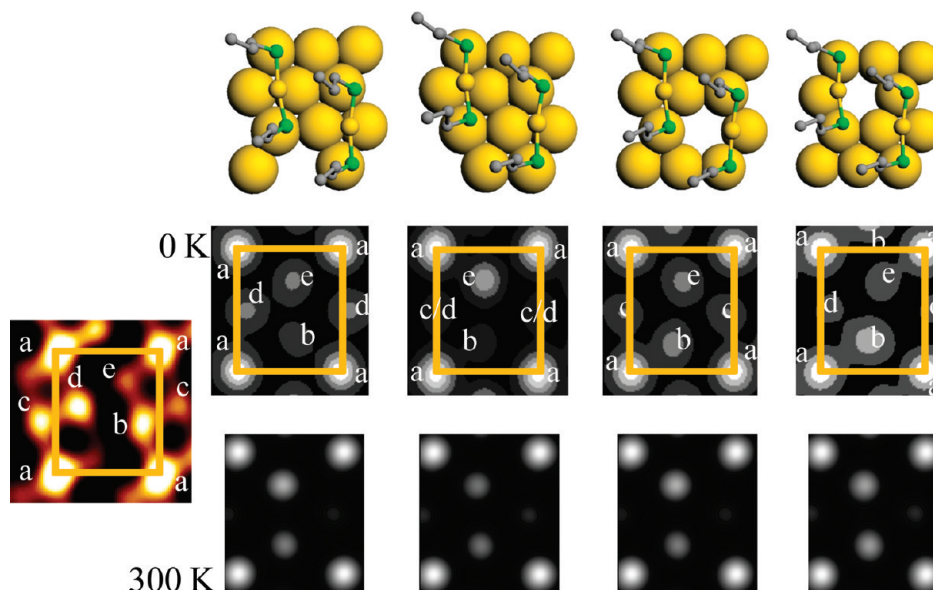


**Figure 6.** Observed in situ STM image of the SAM of 1-propanethiol chemisorbed to the regular Au(111) surface at a coverage of  $\Theta = 1/3$  in the  $(3 \times 2\sqrt{3})$ -4 substrate lattice from Figure 5, left, compared to calculated STM images at 0 and 300 K for four different configurations of a gold surface vacancy. The letters a–e indicate possible assignments of the observed STM features.

(111) surface cell. Using this approach, our results for 1-propanethiol SAMs are consistent with those obtained previously for methanethiol and ethanethiol SAMs,<sup>25</sup> predicting the structure with no local vacancies to be preferred. However, the gold atoms included in adatom layers are actually not initially taken from the bulk metal but instead taken either from the atoms liberated during the lifting of the Au(111) surface reconstruction or else mined from surface pits. Hence; we apply the alternative definition<sup>8</sup>

$$\Delta E_P = (E_{\text{tot}} - E_{\text{surf}} - 4E_{\text{ad}} - nE_{\text{pit}})/4 \quad (3)$$

where  $E_{\text{pit}}$  is the energy required to mine an atom from a pit. We estimate  $E_{\text{pit}}$  as one-quarter of the energy difference between a flat surface and that obtained by removing two adjacent rows (four atoms) from the original eight rows in an  $(8 \times \sqrt{3})$  surface layer. This pit energy is calculated to be  $-0.18$  eV less than the average energy of the bulk atom,<sup>8</sup> making the coalescence of local vacancies into pits a less exothermic process than was previously thought. As shown in Table 2, this enhancement changes the energy balance to make the calculated energies of the structures with no local vacancies and one local vacancy per cell essentially equal. That structures without pits (i.e., effectively bulk atoms are used for the adatoms) are of lower energy than pitted structures is an important property that leads to the commonly observed annealing of pitted surfaces at elevated temperatures.<sup>32</sup>

The anticipated pit coverage on the surface varies from 12.1% for a structure with no local vacancy to 3.8% for a structure with one local vacancy to 4.5% for a structure with two local vacancies (Table 1). By analyzing many STM images previously recorded<sup>30</sup> on large terraces of single-crystal substrates, we deduce the pit coverage to be 4.0%, clearly indicating that the SAM forms with one local vacancy per cell. The pit coverage determined from the presently obtained SAMs of 1-butanethiol is essentially the same, indicating that the interface structure is conserved between 1-propanethiol and 1-butanethiol SAMs. The SAMs of longer alkanethiol SAMs such as octanethiol also have similar pit coverages,<sup>43</sup> while that for methanethiol SAMs is much larger<sup>65</sup> and its interface correspondingly known not to include local vacancies.<sup>22–31,33</sup> On the basis of the images of Dishner et al., Figure 3,<sup>65</sup> we estimate the pit coverage of methanethiol SAMs to be 12–20%, a value that is likely to be an overestimate owing to pit edge effects (as discussed earlier for the striped phase) but nevertheless a good indicator that methanethiol SAMs do not include local vacancies. Also shown in Table 2 are the calculated energies for methanethiol SAM production with 0, 1, or 2 local vacancies. In contrast to the results for 1-propanethiol SAMs for which the 0 and 1 local vacancy energies are essentially equal, the calculations predict that the pit coalescence energy (four times the difference



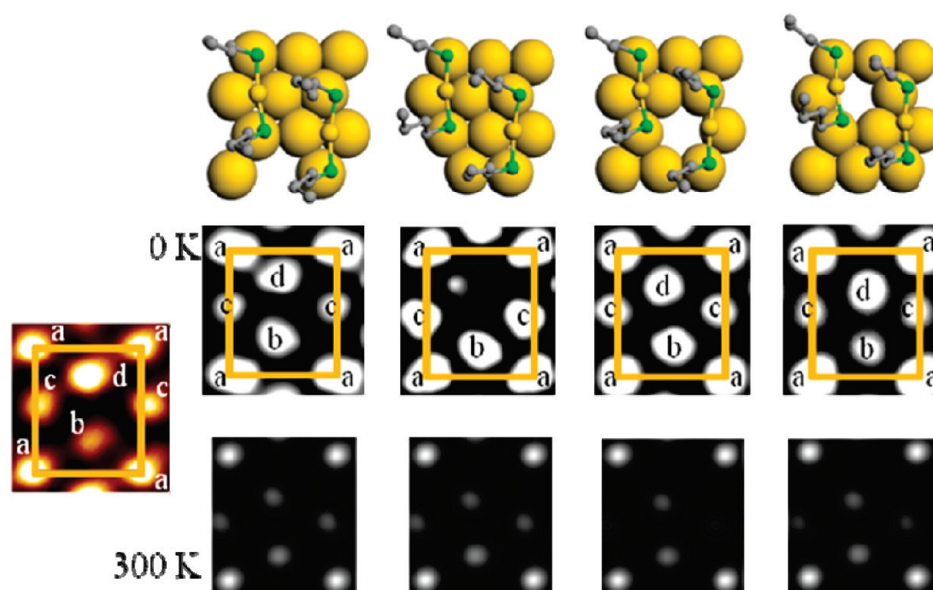


**Figure 7.** Observed in situ STM image of the 1-butanethiol SAM chemisorbed to the regular Au(111) surface at a coverage of  $\Theta = 1/3$  in the  $(3 \times 2\sqrt{3})$ -4 substrate lattice from Figure 5, left, compared to calculated STM images at 0 and 300 K for four different configurations of a gold surface vacancy. The letters a–d indicate possible assignments of the observed STM features.

between the energy of the 1 vacancy per  $(3 \times 2\sqrt{3})$ -4 cell and no-vacancy structure is 0.28 eV for methanethiol, anticipating the observed difference in interface structure. Like the situation already found for the striped phase, it appears that the interface structures of 1-propanethiol and longer linear alkanethiol SAMs are different from that of the most commonly studied alkanethiol SAM, methanethiol.

Further, the high-resolution aspects of the observed STM images of  $(3 \times 2\sqrt{3})$ -4 surface cells of 1-propanethiol and 1-butanethiol SAMs are themselves quite different, as highlighted in Figure 5. The 1-butanethiol SAMs show character similar to other previously reported longer linear alkanethiol SAMs, with four bright spots per cell, whereas the 1-propanethiol SAM displays five bright spots organized in quite a different pattern.

Hence, we simulate the STM images for 1-propanethiol and 1-butanethiol SAMs at  $T = 0$  and at  $T = 300$  K, and the results are compared to the experimental data in Figure 6 (1-propanethiol SAM) and Figure 7 (1-butanethiol SAM). Only the lowest-energy configurations obtained for each of the four possible unique locations of one local vacancy within the cell are presented, configurations that differ in energy at  $T = 0$  by at most 0.1 eV. The optimized coordinates for these structures are provided in the Supporting Information, while the torsional angle probability functions for these simulations are shown in Figure 4. These results indicate that the structures are much more thermally stable than those simulated earlier for the striped phase, though some variation in the S–C–C–C conformations is predicted. The maximum standard deviation in the horizontal motion of the carbon atoms at  $T = 300$  K is calculated to be 0.9 Å, much less than the value of 2 Å predicted for the striped phase. As a result, the structure of the high-density rectangular phase is expected to be less sensitive to solvent effects than the structure of the medium-density striped phase. The simulated STM images for both SAMs at  $T = 0$  do not show the observed intensity patterns, though the SAM for 1-butanethiol does predict spots in all the places that spots are actually observed. Upon heating, three of the four local-vacancy structures develop spot patterns

that closely resemble that observed for the 1-butanethiol SAM, while for the 1-propanethiol SAM, a combination of the STM images calculated for the various vacancy configurations could explain all observed features.

The calculations thus indicate that the unusual observed STM images for the 1-propanethiol SAM originate from averaging over individual images for different vacancy structures. This hypothesis relies on equilibration between the various possible vacancy structures occurring on the STM time scale of ca. 1 s. To test this assumption, the nudged elastic band (NEB) method with eight images is used to determine the transition-state energy for diffusion of a surface vacancy. It is predicted that the energy barrier is 0.74 eV for the shifting of vacancy under the 1-propanethiol SAM. This energy barrier is less than the critical one of 0.82 eV which, according to Redhead's equation<sup>66</sup> with a pre-exponential factor of  $10^{13} \text{ s}^{-1}$ , is required to localize vacancies on this time scale at room temperature. Thus, the surface vacancies are likely to be capable of moving around at room temperature in thiol–gold SAMs, although the calculated barrier is high enough such that experimental variations could induce localization. Indeed, under ultrahigh vacuum conditions, several phases have been observed in single STM images of SAMs of longer alkanethiols such as undecanethiol.<sup>48</sup> This phenomenon has been interpreted as resulting from the tunneling condition of the experiments,<sup>48</sup> but an alternative explanation could be the freezing out of structures associated with specific local vacancies.

Note that all simulations of the high-density rectangular phase prefer a *cis* conformation of the C–S–Au–S–C bonds. Indeed, we calculate this structure to be ca. 0.70 eV lower in energy than the *trans* configuration, in accord with previous theoretical conclusions.<sup>28,29</sup> Differing steric interactions (compare Figure 3 with Figures 6 and 7) prefer instead the *trans* configuration for the striped phase.<sup>31,32</sup> The barrier for isomerization, required for the conversion of the striped phase to the rectangular phase, has been recently estimated to be 0.5 eV.<sup>29,67</sup> At high coverage, this barrier is estimated to be 1.0 eV.<sup>29</sup> All key properties determined for the rectangular phase of the SAMs formed from

methanethiol, 1-propanethiol, and 1-butanethiol are summarized in Table 1.

## 4. CONCLUSIONS

We have studied 1-propanethiol and 1-butanethiol SAMs on Au(111) surfaces by a combination of voltammetry, in situ STM resolved to molecular resolution, and a priori DFT calculations. This combination follows our previous strategy toward similar structural and electronic mapping of both branched alkanethiols and several functionalized alkanethiols.<sup>4,6,7,62</sup> From the deduced atomic-level structure of the observed 1-propanethiol and 1-butanethiol SAMs summarized in Table 1, we see that the low-coverage striped phase and the high-coverage rectangular  $c(4 \times 2)$  phase both involve two adatom-bound R–S–Au–S–R motifs per surface unit cell and one surface vacancy. This conclusion was reached by combining STM measurements of surface pit coverages and surface-cell structure with DFT-simulated STM images at room temperature.

The calculated STM images at 0 K are somewhat insensitive to the location of the surface vacancy within the cell, and the vacancy is likely to be mobile on the surface on the STM time scale at room temperature, particularly for 1-propanethiol. This means that observed images represent an ensemble of surface structures which are, however, more narrowly distributed for 1-butanethiol. Significant adsorbate motion is also anticipated at room temperature, especially for the medium-coverage striped phase, with details of the motion affecting the STM image. The overall packing is, however, more rigid and with fewer vacancy structures for 1-butanethiol than for 1-propanethiol for which the observed images are averaged over different vacancies. This gives ultimately quite different electronic spot patterns for the two molecules in the in situ STM images.

Significantly, all observed interface structures for 1-propanethiol and 1-butanethiol SAMs differ from the corresponding structures for methanethiol SAMs as these involve no local surface vacancies and much larger surface pits. This is rationalized in terms of a ligand-induced reduction of the vacancy coalescence energy for the longer alkyl chains. The SAMs of longer linear alkanethiols appear to follow those for 1-butanethiol, being subtly different from those of 1-propanethiol and significantly different from those of methanethiol.

No intrinsic preference to *cis* or *trans* C–S–Au–S–C conformations is found, with steric forces strongly enforcing different conformations for the striped and rectangular phases. The striped phase thus appears to be stabilized by the large *cis*–*trans* isomerization energy that demands a macroscopic phase change to convert the striped phase to the rectangular phase with increasing coverage.

The combined high-resolution in situ STM images and large-scale state-of-the-art computations point to both striking and subtle differences in the substrate–molecule and intermolecular interactions between the molecules in the SAMs, even for molecules with so closely similar properties as 1-propanethiol and 1-butanethiol (and methanethiol). The differences are likely to fade out when comparison is extended to longer straight alkanethiols. Combined with our recent studies of the branched alkanethiols, 2-methyl-1-propanethiol, both of which display an  $(8 \times \sqrt{3})$ -4 superlattice, R–S–Au–S–R adatom mediated motifs as for 1-propanethiol and 1-butanethiol,<sup>7</sup> and 2-methyl-2-propanethiol, which displays a  $(2\sqrt{7} \times \sqrt{7})R19.1^\circ$ -2 lattice directly on the deconstructed Au(111) surface, no Au-atom

mediating, and no R–S–Au–S–R adatom mediated motifs,<sup>50,68</sup> the present study points to a rich diversity of subtle molecular interactions as well as dynamics of the Au(111) surface itself.<sup>30</sup> Mapping the interface structure to atomic resolution remains in general a challenge but one that is now clearly feasible.

## ■ ASSOCIATED CONTENT

**S Supporting Information.** Tables indicating the accuracy of the approximations used during the MD simulations are provided. Also, the optimized coordinates of the bare unreconstructed Au(111) surfaces, the isolated thiol radicals, and the  $T = 0$  monolayers depicted in Figures 3, 6, and 7 are provided. Finally, the topology of the lowest-energy structures reported in Table 1 and the STM images and their fits used in the development of the high-temperature image simulation approximation are provided. This material is available free of charge via the Internet at <http://pubs.acs.org>.

## ■ AUTHOR INFORMATION

### Corresponding Author

\*E-mail: [ju@kemi.dtu.dk](mailto:ju@kemi.dtu.dk); [reimers@chem.usyd.edu.au](mailto:reimers@chem.usyd.edu.au).

## ■ ACKNOWLEDGMENT

We thank the Australian Research Council for funding Y.W., N.S.H., and J.R.R. under the Discovery Grant program. The use of the supercomputer facilities from National Computer Infrastructure (NCI) and the Australian Centre for Advanced Computing and Communications (AC3) is gratefully acknowledged. Financial support to J.Z., Q.C., and J.U. from the Danish Research Council for Technology and Production Science is acknowledged.

## ■ REFERENCES

- (1) Love, J. C.; Estroff, L. A.; Kriebel, J. K.; Nuzzo, R. G.; Whitesides, G. M. *Chem. Rev.* **2005**, *105*, 1103.
- (2) Vericat, C.; Vela, M. E.; Benitez, G. A.; Gago, J. A. M.; Torrelles, X.; Salvarezza, R. C. *J. Phys.: Condens. Matter* **2006**, *18*, R867.
- (3) Vericat, C.; Vela, M. E.; Salvarezza, R. C. *Phys. Chem. Chem. Phys.* **2005**, *7*, 3258.
- (4) Zhang, J.; Kuznetsov, A. M.; Medvedev, I. G.; Chi, Q.; Albrecht, T.; Jensen, P. S.; Ulstrup, J. *Chem. Rev.* **2008**, *108*, 2737.
- (5) Muller, K. H. *Phys. Rev. B* **2006**, *73*, 045403.
- (6) Bilic, A.; Reimers, J. R.; Hush, N. S. *J. Chem. Phys.* **2005**, *122*, 094708.
- (7) Wang, Y.; Hush, N. S.; Reimers, J. R. *J. Am. Chem. Soc.* **2007**, *129*, 14532.
- (8) Wang, Y.; Chi, Q.; Hush, N. S.; Reimers, J. R.; Zhang, J.; Ulstrup, J. *J. Phys. Chem. C* **2009**, *113*, 19601.
- (9) Reimers, J. R.; Wang, Y.; Cankurtaran, B. O.; Ford, M. J. *J. Am. Chem. Soc.* **2010**, *132*, 8378.
- (10) Andreoni, W.; Curioni, A.; Grönbeck, H. *Int. J. Quantum Chem.* **2000**, *80*, 598.
- (11) Grönbeck, H.; Curioni, A.; Andreoni, W. *J. Am. Chem. Soc.* **2000**, *122*, 3839.
- (12) Hamaguchi, K.; Machida, S.; Mukai, K.; Yamashita, Y.; Yoshinobu, J. *Phys. Rev. B* **2000**, *62*, 7576.
- (13) Vargas, M. C.; Giannozzi, P.; Selloni, A.; Scoles, G. *J. Phys. Chem. B* **2001**, *105*, 9509.
- (14) Yourdshahyan, Y.; Rappe, M. A. *J. Chem. Phys.* **2002**, *117*, 825.
- (15) Gottschalk, J.; Hammer, B. *J. Chem. Phys.* **2002**, *116*, 784.

- (16) Di Felice, R.; Selloni, A.; Molinari, E. *J. Phys. Chem. B* **2003**, *107*, 1151.
- (17) Molina, L. M.; Hammer, B. *Chem. Phys. Lett.* **2002**, *360*, 264.
- (18) Cao, Y.; Ge, Q.; Dyer, D. J.; Wang, L. *J. Phys. Chem. B* **2003**, *107*, 3803.
- (19) Kondoh, H.; Iwasaki, M.; Shimada, T.; Amemiya, K.; Yokoyama, T.; Ohta, T. *Phys. Rev. Lett.* **2003**, *90*, 066102.
- (20) Roper, M. G.; Skegg, M. P.; Fisher, C. J.; Lee, J. J.; Dhanak, V. R.; Woodruff, D. P.; Jones, R. G. *Chem. Phys. Lett.* **2004**, *389*, 87.
- (21) Yu, M.; Bovet, N.; Satterley, C. J.; Bengio, S.; Lovelock, K. R. J.; Milligan, P. K.; Jones, R. G.; Woodruff, D. P.; Dhanak, V. *Phys. Rev. Lett.* **2006**, *97*, 166102.
- (22) Grönbeck, H.; Odelius, M. *Phys. Rev. B* **2010**, *82*, 085416.
- (23) Mazzarello, R.; Cossaro, A.; Verdini, A.; Rousseau, R.; Casalis, L.; Danisman, M. F.; Floreano, L.; Scandolo, S.; Morgante, A.; Scoles, G. *Phys. Rev. Lett.* **2007**, *98*, 16102.
- (24) Maksymovych, P.; Sorescu, D. C.; Yates, J. T., Jr. *Phys. Rev. Lett.* **2006**, *97*, 146103.
- (25) Torres, E.; Blumenau, A. T.; Biedermann, P. U. *Phys. Rev. B* **2009**, *79*, 075440.
- (26) Li, F. S.; Zhou, W. C.; Guo, Q. M. *Phys. Rev. B* **2009**, *79*, 113412.
- (27) Kautz, N. A.; Kandel, S. A. *J. Am. Chem. Soc.* **2008**, *130*, 6908.
- (28) Grönbeck, H.; Häkkinen, H.; Whetten, R. L. *J. Phys. Chem. C* **2008**, *112*, 15940.
- (29) Jiang, D. E.; Dai, S. *Phys. Chem. Chem. Phys.* **2009**, *11*, 8601.
- (30) Zhang, J.; Chi, Q.; Ulstrup, J. *Langmuir* **2006**, *22*, 6203.
- (31) Voznyy, O.; Dubowski, J. J.; Yates, J. T.; Maksymovych, P. *J. Am. Chem. Soc.* **2009**, *131*, 12989.
- (32) Mehring, P.; Beimborn, A.; Westphal, C. *App. Surf. Sci.* **2010**, *256*, 7265.
- (33) Sheppard, D. C.; Parkinson, G. S.; Hentz, A.; Window, A. J.; Quinn, P. D.; Woodruff, D. P.; Bailey, P.; Noakes, T. C. *Q. Surf. Sci.* **2011**, *605*, 138.
- (34) Jadzinsky, P. D.; Calero, G.; Ackerson, C. J.; Bushnell, D. A.; Kornberg, R. D. *Science* **2007**, *318*, 430.
- (35) Zhu, M.; Aikens, C. M.; Hollander, F. J.; Schatz, G. C.; Jin, R. *J. Am. Chem. Soc.* **2008**, *130*, 5883.
- (36) Fischer, D.; Curioni, A.; Andreoni, W. *Langmuir* **2003**, *19*, 3567.
- (37) Zhang, J.; Chi, Q.; Nielsen, J. U.; Friis, E. P.; Andersen, J. E. T.; Ulstrup, J. *Langmuir* **2000**, *16*, 7229.
- (38) Arce, F. T.; Vela, M. E.; Salvarezza, R. C.; Arvia, A. J. *Langmuir* **1998**, *14*, 7203.
- (39) Arce, F. T.; Vela, M. E.; Salvarezza, R. C.; Arvia, A. J. *J. Chem. Phys.* **1998**, *109*, 5703.
- (40) Poirier, G. E.; Fitts, W. P.; White, J. M. *Langmuir* **2001**, *17*, 1176.
- (41) Esplandiú, M. J.; Hagenstrom, H.; Kolb, D. M. *Langmuir* **2001**, *17*, 828.
- (42) Yamada, R.; Uosaki, K. *Langmuir* **1998**, *14*, 855.
- (43) Poirier, G. E. *Langmuir* **1997**, *13*, 2019.
- (44) Grönbeck, H.; Häkkinen, H. *J. Phys. Chem. B* **2007**, *111*, 3325.
- (45) Nagoya, A.; Morikawa, Y. *J. Phys.: Condens. Matter* **2007**, *19*, 365245.
- (46) Wang, J. G.; Selloni, A. *J. Phys. Chem. C* **2007**, *111*, 12149.
- (47) Cossaro, A.; Mazzarello, R.; Rousseau, R.; Casalis, L.; Verdini, A.; Kohlmeier, A.; Floreano, L.; Scandolo, S.; Morgante, A.; Klein, M. L.; Scoles, G. *Science* **2008**, *321*, 943.
- (48) Riposan, A.; Liu, G. Y. *J. Phys. Chem. B* **2006**, *110*, 23926.
- (49) Chen, W.; Madhavan, V.; Jamneala, T.; Crommie, M. F. *Phys. Rev. Lett.* **1998**, *80*, 1469.
- (50) Min, B. K.; Alemozafar, A. R.; Biener, M. M.; Biener, J.; Friend, C. M. *Top. Catal.* **2005**, *36*, 77.
- (51) Barth, J. V.; Brune, H.; Ertl, G.; Behm, R. J. *Phys. Rev. B* **1990**, *42*, 9307.
- (52) Wang, Y.; Hush, N. S.; Reimers, J. R. *Phys. Rev. B* **2007**, *75*, 233416/1.
- (53) Kresse, G.; Hafner, J. *Phys. Rev. B* **1993**, *47*, 558.
- (54) Vanderbilt, D. *Phys. Rev. B* **1990**, *41*, 7892.
- (55) Kresse, G.; Hafner, J. *J. Phys.: Condens. Matter* **1994**, *6*, 8245.
- (56) Perdew, J. P.; Wang, Y. *Phys. Rev. B* **1992**, *45*, 13244.
- (57) Bilic, A.; Reimers, J. R.; Hush, N. S.; Hafner, J. *J. Chem. Phys.* **2002**, *116*, 8981.
- (58) Neugebauer, J.; Scheffler, M. *Phys. Rev. B* **1992**, *46*, 16067.
- (59) Makov, G.; Payne, M. C. *Phys. Rev. B* **1995**, *51*, 4014.
- (60) Wang, Y.; Hush, N. S.; Reimers, J. R. *J. Phys. Chem. C* **2007**, *111*, 10878.
- (61) Marx, D.; Hutter, J. *Ab initio Molecular Dynamics: Basic Theory and Advanced Methods*; Cambridge University Press: Cambridge, 2009.
- (62) Zhang, J.; Bilic, A.; Reimers, J. R.; Hush, N. S.; Ulstrup, J. *J. Phys. Chem. B* **2005**, *109*, 15355.
- (63) Tersoff, J.; Hamann, D. R. *Phys. Rev. Lett.* **1998**, *1983*, 50.
- (64) Chi, Q.; Zhang, J.; Andersen, J. E. T.; Ulstrup, J. *J. Phys. Chem. B* **2001**, *105*, 4669.
- (65) Dishner, M. H.; Hemminger, J. C.; Feher, F. J. *Langmuir* **1997**, *13*, 2318.
- (66) Redhead, P. A. *Vacuum* **1962**, *12*, 203.
- (67) Jiang, D. E.; Dai, S. *Inorg. Chem.* **2009**, *48*, 2720.
- (68) Chi, Q.; Zhang, J.; Ulstrup, J. *J. Phys. Chem. B* **2006**, *110*, 1102.